Original contribution

STrategically Acquired Gradient Echo (STAGE) imaging, part I: Creating enhanced T1 contrast and standardized susceptibility weighted imaging and quantitative susceptibility mapping

Yongsheng Chen[a, b, c], Saifeng Liu[b], Yu Wang[d], Yan Kang[a], E. Mark Haacke[a, b, c, d, *]

[a] *Sino-Dutch Biomedical and Information Engineering School, Northeastern University, Shenyang, China*
[b] *The MRI Institute for Biomedical Research, Detroit, MI, USA*
[c] *Department of Radiology, School of Medicine, Wayne State University, Detroit, MI, USA*
[d] *Shanghai Key Laboratory of Magnetic Resonance Imaging, East China Normal University, Shanghai, China*

ARTICLE INFO

ABSTRACT

Purpose: To provide whole brain grey matter (GM) to white matter (WM) contrast enhanced T1W (T1WE) images, multi-echo quantitative susceptibility mapping (QSM), proton density (PD) weighted images, T1 maps, PD maps, susceptibility weighted imaging (SWI), and R2* maps with minimal misregistration in scanning times < 5 min.
Methods: Strategically acquired gradient echo (STAGE) imaging includes two fully flow compensated double echo gradient echo acquisitions with a resolution of $0.67 \times 1.33 \times 2.0 \text{ mm}^3$ acquired in 5 min for 64 slices. Ten subjects were recruited and scanned at 3 Tesla. The optimum pair of flip angles (6° and 24° with TR = 25 ms at 3T) were used for both T1 mapping with radio frequency (RF) transmit field correction and creating enhanced GM/WM contrast (the T1WE). The proposed T1WE image was created from a combination of the proton density weighted (6°, PDW) and T1W (24°) images and corrected for RF transmit field variations. Prior to the QSM calculation, a multi-echo phase unwrapping strategy was implemented using the unwrapped short echo to unwrap the longer echo to speed up computation. R2* maps were used to mask deep grey matter and veins during the iterative QSM calculation. A weighted-average sum of susceptibility maps was generated to increase the signal-to-noise ratio (SNR) and the contrast-to-noise ratio (CNR).
Results: The proposed T1WE image has a significantly improved CNR both for WM to deep GM and WM to cortical GM compared to the acquired T1W image (the first echo of 24° scan) and the T1MPRAGE image. The weighted-average susceptibility maps have $80 \pm 26\%$, $55 \pm 22\%$, $108 \pm 33\%$ SNR increases for the ten datasets compared to the single echo result of 17.5 ms, and $80 \pm 36\%$, $59 \pm 29\%$ and $108 \pm 37\%$ CNR increases for the putamen, caudate nucleus, and globus pallidus, respectively.
Conclusions: STAGE imaging offers the potential to create a standardized brain imaging protocol providing four pieces of quantitative tissue property information and multiple types of qualitative information in just 5 min.

1. Introduction

Fast three-dimensional (3D) gradient echo (GRE) [1–4] imaging has been widely used for producing whole brain T1 weighted (T1W) and proton density weighted (PDW) images. Using multiple flip angles (FAs), it can be used to create T1 and PD maps over and above the usual T2* maps when multi-echo data are collected. These images provide essential anatomical and quantitative information of brain tissues for studying various neurodegenerative diseases [5–12]. In addition, the visualization of tissues with different susceptibilities (e.g. cerebral veins, microbleeds, and calcification) in GRE data can be enhanced using susceptibility weighted imaging (SWI) [13,14], through the utilization of the phase information [15–24]. Furthermore, quantitative susceptibility mapping (QSM) can be generated to quantify local susceptibilities in a geometry and orientation independent fashion [25–29],

with the ability to differentiate iron from calcification [26–31]. Moreover, multi-parametric and quantitative magnetic resonance imaging (qMRI) approaches such as DESPOT [32,33], synthetic MRI [34–37] and MR fingerprinting [38,39] show the current interest of quantifying T1, proton density and T2*.

However, these various qualitative and quantitative images are normally acquired in separate scans which lead to a long scanning time and possible image misregistration. Furthermore, the T1W image from a GRE sequence with a single flip angle (FA) yields limited grey matter (GM) and white matter (WM) contrast and has inherent image inhomogeneity from both the RF transmit (B_{1t}) and receiver coil signal response variations (B_{1r}). Insufficient GM/WM contrast and RF inhomogeneity increase the complexity of automatic brain structure segmentation from T1W images [40–42]. Nowadays, the inversion recovery prepared T1W, Magnetization Prepared Rapid Acquisition of Gradient Echoes (T1MPRAGE), is preferred over conventional GRE sequence without any magnetization preparation to get improved T1 contrast. As it employs a smaller FA, T1MPRAGE could have more B_{1t} inhomogeneity than the GRE which uses a lager FA. Finally, QSM at longer echo times (TE) can suffer from phase aliasing although data from long echo times are more sensitive to small changes in susceptibility. Therefore, we propose to also use short TE for better quantification of susceptibility when high iron content is present even though the signal-to-noise ratio (SNR) may be less than the results from a longer TE.

To address these problems, and to develop a rapid imaging protocol to provide whole brain coverage, we introduce a STrategically Acquired Gradient Echo (STAGE) imaging approach to create T1W images, PDW images, T1 map, PD map, R2* map, SWI, true-SWI (or tSWI) images [43], enhanced T1W contrast (T1WE) between GM and WM and improved multi-echo QSM data (ME-QSM). In STAGE Part II, a novel T1 mapping and RF transmit and receive field correction method using two flip angles is presented. In this paper, STAGE Part I, we introduce the enhanced T1W contrast and multi-echo data acquisition and calculation for ME-QSM.

2. Material and methods

2.1. STAGE concepts

STAGE includes two double-echo GRE scans employing a pair of optimal flip angles, one being smaller than the Ernst angle of WM and the other larger than the Ernst angle, to produce PDW (FA = 6°) and T1W (FA = 24°) images, respectively. As shown in many studies [32,33,44–47], two optimum flip angles can be used to quantify whole brain T1 and PD. In our study, the two short echoes in each scan are used for the T1 and PD mapping after RF field correction, which is introduced in the STAGE Part II paper. All four echoes are used to create a T1WE image with enhanced GM/WM contrast and improved image homogeneity by subtracting the B_{1t} corrected PDW image from the T1W image for both short and long echoes. Then the two T1WE images are averaged to generate the final T1WE image with improved GM/WM contrast-to-noise ratio (CNR), SNR and image homogeneity. The four echo times are optimized in terms of their echo times for addressing the ME-QSM reconstructions. All echoes are fully flow compensated by nulling the zero- and first-order gradient moments for each echo independently [48]. Both SWI and tSWI can be generated from the second echo of the low flip angle scan. Furthermore, one can also use the SWI and tSWI generated from the first echo for thrombosis detection [23,49]. R2* maps are generated from each of the flip angle images then averaged.

2.2. Theory and simulations

For an ideal steady-state RF spoiled GRE data acquisition, the acquired signal as a function of flip angle (θ) is given by the well-known Ernst equation,

$$S(\theta) = \rho_0 \cdot \sin\theta \cdot \frac{1 - E_1}{1 - \cos\theta \cdot E_1} \cdot E_2 \tag{1}$$

where ρ_0 is the proton density, $E_1 = e^{-TR/T1}$, $E_2 = e^{-TE/T2*}$, TR is the repetition time, TE is the echo time, and T1 and T2* are the longitudinal and transverse relaxation times. As known from Eq. (1), an FA smaller than the Ernst angle of WM gives a PDW image whereas an FA larger than the Ernst angle gives a T1W image. However, the contrast between GM and WM given by one FA is restricted by the intrinsic T1 ratio of GM and WM. Since there are images with two FAs, novel contrast can be obtained by a combination of the data. One such approach is to subtract the PDW image (or a scaled version of it) from the T1W image. The GM/WM CNR from Eq. (1) can be written as:

$$CNR_{gre} = \frac{|S_{WM}(\theta) - S_{GM}(\theta)|}{\sigma_0} \tag{2}$$

where $S_{WM,GM}$ are signal mean values for WM and GM on a given region, σ_0 is the image noise standard deviations (SD) that common to both tissues WM and GM, θ is the FA, and the symbol || represents taking the absolute value. If an image is created by the subtraction of two signals, the σ_0 would be replaced by $\sqrt{2}\sigma_0$. Therefore, the GM/WM CNR of the subtraction between two signals with different FAs (θ_1, θ_2) from Eq. (1) can be written as:

$$
\begin{aligned}
&CNR_{sub} \\
&= \frac{|(S_{WM}(\theta_2) - S_{WM}(\theta_1)) - (S_{GM}(\theta_2) - S_{GM}(\theta_1))|}{\sqrt{2}\sigma_0}
\end{aligned} \tag{3}
$$

To confirm the expected CNR increase by the subtraction, we performed the simulation for Eqs. (1)–(3) with the following parameters from the literature [22]: TR = 25 ms, TE = 7.5 ms, PD_{GM} = 0.84, $T1_{GM}$ = 1600 ms, $T2*_{GM}$ = 66 ms, PD_{WM} = 0.68, $T1_{WM}$ = 900 ms and $T2*_{WM}$ = 50 ms. WM and GM images were generated across FA from 1° to 90° respectively. For a theoretical simulation of Eqs. (1)–(3), we did not add noise for the simulated WM and GM signals, instead we use σ_0 = 1 is for each simulated signal. S_{WM}, S_{GM}, CNR_{gre} and CNR_{sub} were plotted as a function of FA (Fig. 1). The θ_2 for a given θ_1 was given by holding θ_1 fixed and searching for θ_2 from 1° to 90° in order to maximize CNR_{sub} using Eq. (3). From the simulation, the CNR_{sub} is larger than the CNR_{gre} at each FA.

On the other hand, as demonstrated in Deoni's study [50], the precision of whole brain T1 mapping by two FAs can be described by the product of the dynamic range (DR) of the regression line and the fractional signal of the points (FS), given by:

$$DR \times FS = \left[\frac{S(\theta_2)}{\rho_0 \sin\theta_2} - \frac{S(\theta_1)}{\rho_0 \sin\theta_1} \right] \times \left[\frac{S(\theta_1) + S(\theta_2)}{2S(\theta_E)} \right] \tag{4}$$

where θ_E is the Ernst angle of WM with given TR and T1. The study proposed that the optimum T1 precision will be achieved when the DR × FS is maximized. However, the pair of FAs for maximizing T1 precision (DR × FS) may not be the same with the pair of FAs maximizing the contrast between GM and WM (CNR_{sub}). We propose the optimum pair of FAs for the two purposes of STAGE, increasing GM/WM contrast and maximizing T1 precision, will be achieved when the sum of CNR_{sub} and DR × FS is maximized. The CNR_{sub}, the DR × FS and the sum of them were plotted using 2D contour plots (Fig. 2) based on the previous described simulation. Any pair of FAs sitting in the 90% of the maximum summed value (the highest contour on Fig. 2c) can do a desired job for STAGE purposes. The maximum CNR_{sub} was achieved at $\theta_1 = 4°$, $\theta_2 = 24°$. The maximum DR × FS was achieved at $\theta_1 = 6°$, $\theta_2 = 33°$. Since an FA = 6° has a better image SNR than an FA = 4°, and an FA = 24° has a lower Specific Absorption Rate (SAR)
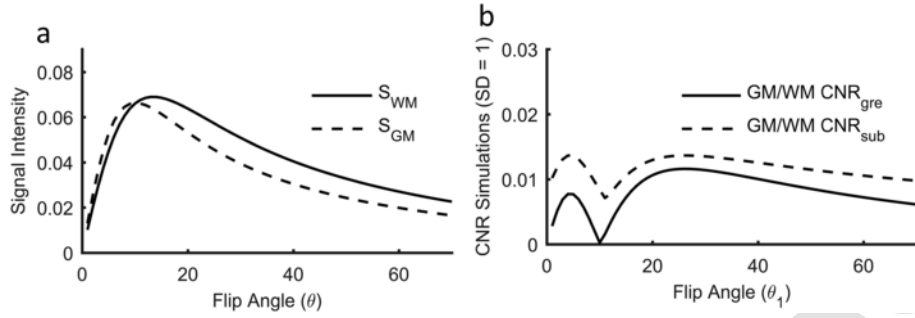
Fig. 1. Simulation of signal variation and CNR as a function of flip angle. (a) S_{WM} and S_{GM} are given by Eq. (1). (b) CNR_{gre} is from Eq. (2) and CNR_{sub} is from Eq. (3). The simulation uses $\sigma_0 = 1$ for each signal. The CNR_{sub} is larger than the CNR_{gre} at each FA with the given imaging parameters. The maximum CNR_{sub} is achieved at $\theta_1 = 4°$, $\theta_2 = 24°$.
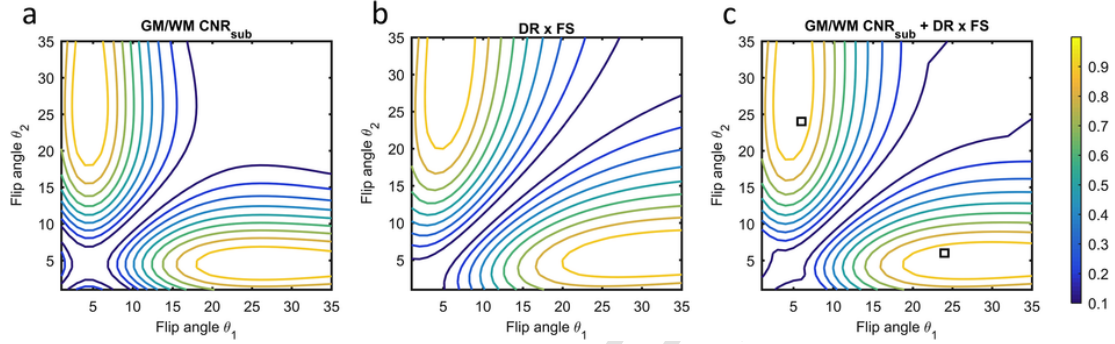

Fig. 2. Contour plots of the CNR_{sub}, DR × FS and the sum of them as a function of θ_1 and θ_2 to determine the two FAs for STAGE. For CNR purposes (a), the optimum angles are $\theta_1 = 4°$, $\theta_2 = 24°$. For T1 precision (b), the optimum angles are $\theta_1 = 6°$, $\theta_2 = 33°$. We use $\theta_1 = 6°$, $\theta_2 = 24°$ (squares on c) for in vivo studies which are sitting in the 90% region of the maximum value of the sum. Values on a, b and c were normalized to 1.

than FA = 33°, we use $\theta_1 = 6°$, $\theta_2 = 24°$ for in vivo studies (squares on Fig. 2c).

Including the effects of RF inhomogeneity, the GRE data acquisition can be written as:

$$S'(\theta) = \rho_0 \cdot bias \cdot k \cdot \sin(k\theta) \cdot \frac{1 - E_1}{1 - \cos(k\theta) E_1} \cdot E_2 \tag{5}$$

where k represents the deviation from B_{1t} field non-uniformity and *bias* represents the B_{1r} field variation. Both k and *bias* are position related. Therefore, a given tissue may exhibit different signal intensity at different positions because of B_{1r} and B_{1t} spatial variations. Known from Eq. (5), an FA smaller than the Ernst angle of WM suffers more B_{1t} field variation than an FA lager than the Ernst angle. We define the T1WE image by the linear subtraction (LS) between the higher flip angle and the corrected lower flip angle as:

$$S_{T1WE} = S'(\theta_2, TE_n) - \lambda S'(\theta_1, TE_n) \tag{6}$$

where $\theta_1 = 6°$ provides a PDW image, $\theta_2 = 24°$ provides a T1W image, $\lambda = 1/k^\alpha$, with k the extracted B_{1t} field variation, α is a constant and TE_n is the nth echo. Since both scans are double-echo scans, the final T1WE image is given by the average between the two T1WE images calculated from Eq. (6) using the first and second echoes.

To demonstrate this point and determine the constant (α) for generating T1WE, we performed a simulation for Eqs. (5), (6) using the same parameters of the previous simulation and with k ranging from 0.6 to 1.3. The B_{1r} field variation (*bias*) was ignored during the simulation as it is often corrected by the manufacturer. The signal intensity at the two selected FAs and the T1WE as a function of k were plotted for WM and GM respectively (Fig. 3). From the simulation, both WM and GM suffer more B_{1t} field variation on the PDW (FA = 6°) than the T1W
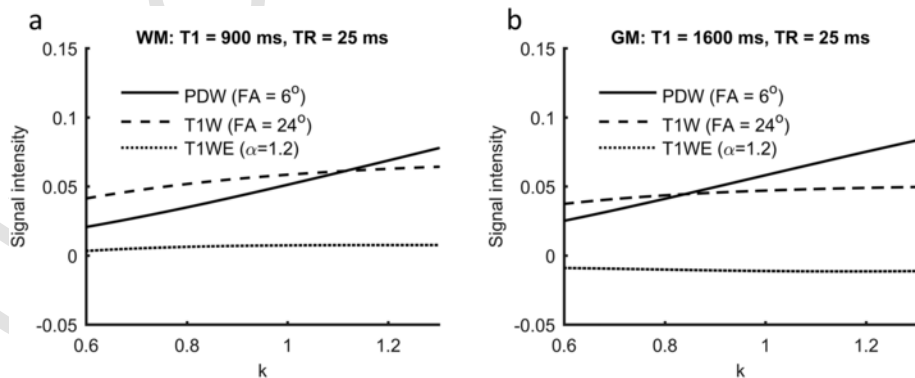

Fig. 3. Simulation of signal intensity as a function of k for WM (a) and GM (b). PDW and T1W are from Eq. (5) with *bias = 1*. The PDW suffers more inhomogeneity than the T1W for both GM and WM. T1WE is from Eq. (6) with $\alpha = 1.2$ which has a more uniform signal than PDW and T1W across k values.

(FA = 24°) across different k values. The T1WE image generated form Eq. (6) with α = 1.2 presents a flat signal across different k values.

2.3. In vivo data acquisition and data processing

Ten healthy volunteers were recruited and the study was approved by the local Institutional Review Board with written consent from each volunteer obtained prior to the scan. All scans were performed on a Siemens Verio 3T scanner (Siemens Healthcare, Erlangen, Germany)

Table 1
STAGE imaging parameters for 3T.

	Axial DE PDW	Axial DE T1W
FOV (mm) × Phase FOV	256 × 75%	
Scanning matrix	384 × 144	
Slice thickness (mm)	2.0	
Voxel size (mm³)	0.67 × 1.33 × 2.0	
Number of slices	64	
Slice oversampling	12.5%	
TR (ms)	25	
TE (ms)	7.5/17.5	8.75/18.75
FA (degree)	6	24
Pixel BW (Hz/pixel)	240	
Flow compensation[a]	Yes	
Acc. factor (GRAPPA)	2	
TA (min:sec)	2:29	2:29

[a] *Yes* means full flow compensation in all three orthogonal directions.

with imaging parameters described in Table 1. The total scan time for the two scans was 5 min. For comparison purposes, an additional T1MPRAGE scan was acquired at the same time for all subjects with the same imaging parameters as STAGE scans for spatial resolution, parallel imaging acceleration and slice locations. With TR = 1200 ms, TE = 2.82 ms, FA = 9°, and BW/pixel = 180 Hz/pixel, the T1MPRAGE scanning time was 1 min and 40 s. The 'Pre-scan normalize' option provided by the vendor was used for all scans to correct B_{1r} field variations.

An in-house program was developed using MATLAB (MathWorks, Natick, MA) to process the data and generate all results automatically. The whole data processing workflow is shown in Fig. 4.

The T1, PD and k maps were calculated from the two first echoes using the proposed method described in the STAGE Part II paper. After correcting for the transmit field variations, the resulting PDW image was subtracted from the T1W image for each of the two echoes and the two T1WE images were averaged. A constant was added to the T1WE image to avoid negative values. SWI and tSWI were generated from the second echo of the 6° scan. R2* maps were calculated using the two echoes for each scan, then averaged.

The four echo times of 7.5 ms/17.5 ms from the 6° scan and 8.75 ms/18.75 ms from the 24° scan were chosen specifically for use in our ME-QSM reconstruction approach. With the phase images at 7.5 ms unwrapped using the quality guided 3D phase unwrapping algorithm (3DSRNCP) [51], the 1.25 ms increase in TE (ΔTE) from the 6° to the 24° scan makes it possible to avoid aliasing and unwrap the phase images at 8.75 ms rapidly given by:
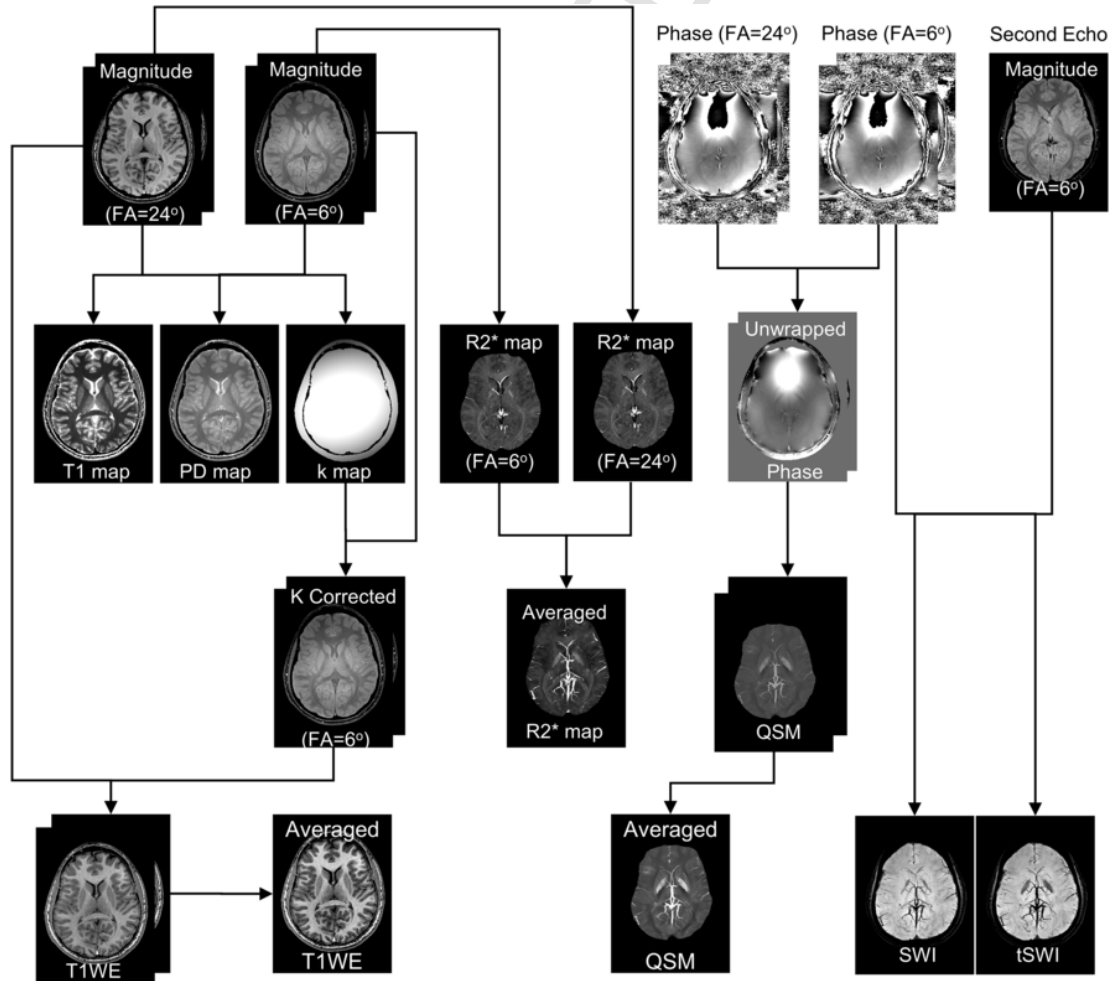

Fig. 4. STAGE data processing workflow. The calculations for T1 map, PD map and k map are introduced in STAGE part II.

$$\varphi_{uw}\left(TE_n\right) = \varphi\left(TE_n\right)$$
$$- \left[\frac{\varphi\left(TE_n\right) - \varphi_{uw}\left(TE_{n-1}\right) \times \frac{TE_n}{TE_{n-1}}}{2\pi} \right] \times 2\pi \qquad (7)$$

where φ_{uw} is the unwrapped phase, φ is the original phase at each echo and [] is the rounding operator. After that, phase images with an effective TE of 16.25 ms are created by adding the two unwrapped phase images of 7.5 ms and 8.75 ms to unwrap those at 17.5 ms. Finally, the phase images at 18.75 ms can be unwrapped using the unwrapped phase images at 17.5 ms using Eq. (7). A brain extraction tool (BET) [52] was used to generate the brain mask and this mask was adjusted further using the phase image quality map [53] which removes regions with rapid phase changes. The masked phase images at each echo time were processed using Sophisticated Harmonic Artifact Reduction for Phase data (SHARP) [54] to remove the background field and then QSM images generated for each echo using the truncated k-space division algorithm [55]. The R2* map calculated from the two echoes in the 6° scan is used as an additional geometry mask for deep GM and veins during the iterative QSM calculation. In iterative QSM, a geometry mask of the veins and grey matter structures is generated by thresholding the original QSM image with a threshold = 0.15 ppm. Then another geometry mask is generated from the R2* map with a threshold = 0.05 s^{-1} to further improve the accuracy of the geometry mask for deep GM structures and major veins. After the QSM data are obtained for each echo, a combined QSM is generated thorough weighted averaging of all single echo QSM images to improve the SNR of the final QSM image. The averaging weights are given by Eq. (8), where M_n and TE_n are the magnitude image intensity and echo time of each echo.

$$Weight_n = \frac{M_n^2 * TE_n^2}{\sum_{n=1}^{4} \left(M_n^2 * TE_n^2 \right)} \qquad (8)$$

To evaluate the improvement of the T1WE image compared to the T1W image (the first echo with FA = 24°) and the T1MPRAGE image, the CNR of WM to deep GM and WM to cortical GM were measured for all ten datasets. For each dataset, three regions-of-interest (ROI) were drawn on the T1WE image at the middle slice showing putamen and caudate nucleus. These ROIs were then copied to the same slice of the T1W image and the T1MPRAGE image using SPIN-LITE software (MR Innovations, Detroit, USA). The ROIs chosen were: ROI$_1$ = the WM area on the right side of the genu of the corpus callosum without including any GM or visible blood vessels; ROI$_2$ = the right-side putamen; ROI$_3$ = the cortical gyri beside ROI$_1$. Images were zoomed four times to draw the ROI on the cortical gyri more precisely. ROI$_1$ represents WM, ROI$_2$ represents deep GM and ROI$_3$ represents cortical GM. The CNR between two tissues given by Eq. (2) was calculated on each image of T1W, T1MPRAGE and final T1WE respectively. The SD of ROI$_1$ (the WM ROI) was used as the image noise SD (σ_0) for T1W, T1MPRAGE and T1WE, since the SD for T1WE was measured on the resultant T1WE image. Measured CNRs were expressed as mean ± SD over all the ten datasets. One-way ANOVA followed by the Tukey-Kramer post hoc test was performed to compare T1W to T1WE, and T1MPRAGE to T1WE for WM to deep GM and WM to cortical GM, respectively. Here $p < 0.05$ was considered significant and $p < 0.005$ highly significant.

To demonstrate the improvement in image homogeneity on the T1WE image compared to the T1W image and the T1MPRAGE image, the histogram of the same slice for the CNR measurement was plotted on BET extracted brain images along with the sagittal view and coronal view of the axial images.

To evaluate the quality of the weighted-average QSM image compared to the single echo QSM image with TE = 17.5 ms, SNR and CNR of putamen (PUT), caudate nucleus (CN) and globus pallidus (GP) were measured using manually drawn ROIs on the right-side (S_r) and left-side (S_l) structures at the same slice location which was used for measuring magnitude image CNR. The QSM image has major susceptibility variations in the basal ganglia structures, while the WM has relatively more uniform susceptibility. Using SD from each ROI for QSM SNR and CNR calculation gives the fact that there could be some spatial variation in the images is an over-estimate of the true SD. Therefore, the mean (S_0) and SD (σ_0) of the WM ROI was used to provide the background signal and image noise SD for the QSM images. The SNR_{QSM} and CNR_{QSM} are defined by:

$$SNR_{QSM} = \frac{\mid \left(S_r + S_l \right) \mid}{2\sigma_{WM}} \qquad (9)$$

$$CNR_{QSM} = \frac{\mid \left(S_r + S_l \right) - 2S_{WM} \mid}{2\sigma_{WM}} \qquad (10)$$

Then the SNR and CNR increases for weighted-average QSM compared to single echo QSM were plotted for each structure across the ten datasets.

3. Results

The RF corrected T1WE image showed clear GM/WM contrast improvement not only at the top of the brain and for the basal ganglia structures but also for GM/WM in the sulci as well (Fig. 5 and Fig. 6). This is well demonstrated in the histogram profile showing a clear separation in signal for the WM and GM after RF correction (Fig. 5c) compared to that from the T1W (Fig. 5a) and T1MPRAGE (Fig. 5b) images. The T1WE images also showed improved homogeneity in the partition direction where the T1MPRAGE had rather large variations at the beginning and ending slices (Fig. 6 slices 10, 13 and 53 on the T1MPRAGE row). The measured CNRs on the T1WE image were 13.7 ± 4.2 and 23.5 ± 5.4 for WM to deep GM and WM to cortical GM, compared to the T1W images which were 4.9 ± 1.8 and 17.9 ± 4.0 and the T1MPRAGE images which were 1.4 ± 0.8 and 15.7 ± 4.3. As shown in Fig. 7, the T1WE image has significant CNR improvement than the T1W image ($p = 0.0001$ and $p = 0.0159$) and the T1MPRAGE ($p = 0.0001$ and $p = 0.0021$) both for WM to deep GM and WM to cortical GM.

Using the proposed phase unwrapping algorithm, it took only 14 s to unwrap all four echoes, compared to 47 s using the 3DSRNCP unwrapping algorithm for each echo on the same computer. All pixels were unwrapped correctly on all datasets (Fig. 8). The weighted-average susceptibility maps have 80 ± 26%, 55 ± 22%, 108 ± 33% SNR increases for the ten datasets compared to the single echo result of 17.5 ms, and 80 ± 36%, 59 ± 29% and 108 ± 37% CNR increases for the PUT, CN, and GP, respectively (Fig. 9).

A STAGE case with all those resulting images is shown in Fig. 10.

4. Discussion

The multi-parametric and qMRI approaches have great potential for studying various neurodegenerative diseases. With the proposed STAGE imaging approach, one can acquire whole brain information in a few minutes including: PDW images, T1W images, T1WE images, T1 map, PD map, R2* map, SWI, true SWI, and improved ME-QSM data. In case there is no magnetic resonance angiography (MRA) scan performed, an approximate MRA can also be generated using the first echo of the 24° scan since this echo is fully flow compensated. It shows sufficient in-flow effect for major arteries such as the internal carotid arteries and middle cerebral arteries. The fact that these two scans are ac-
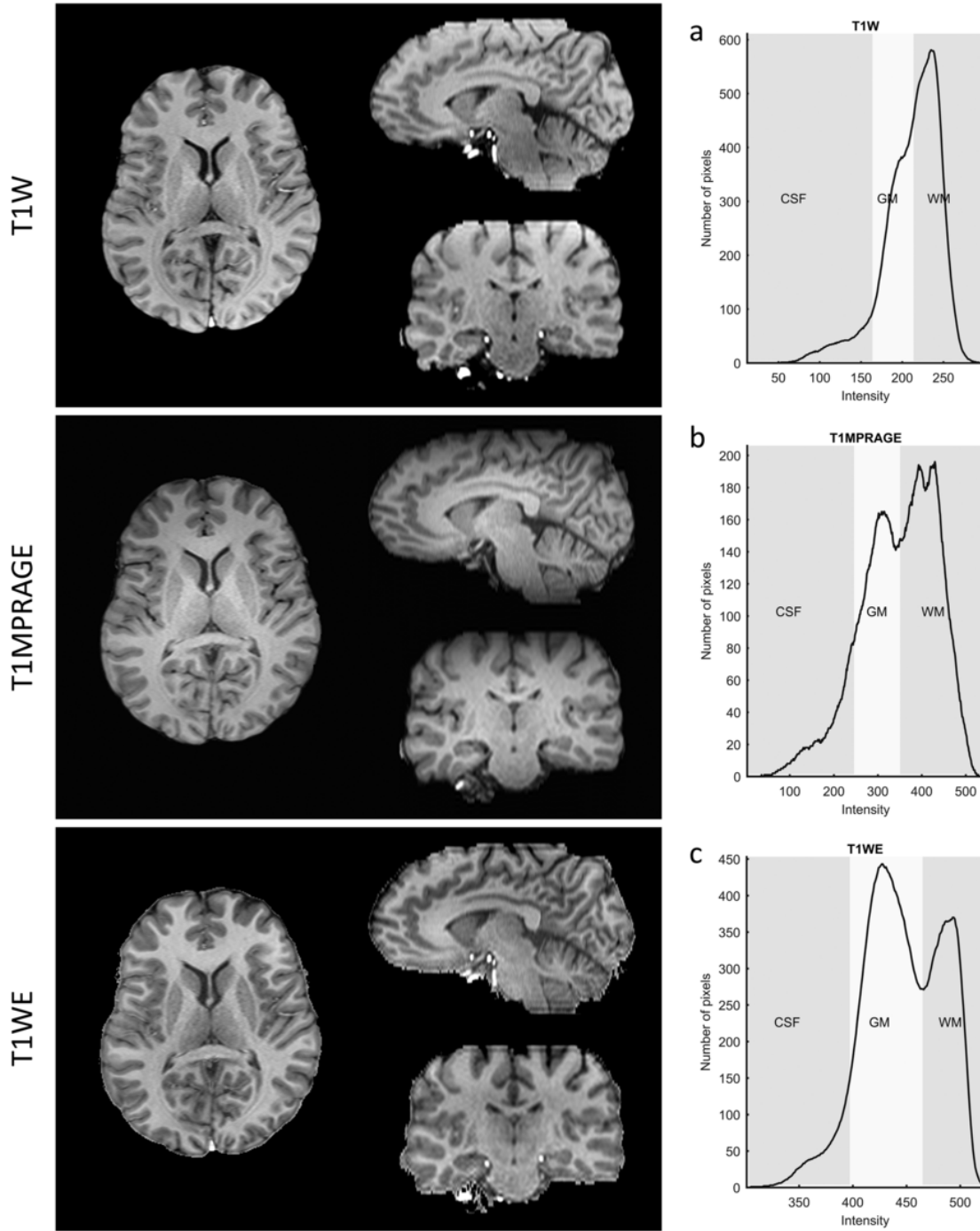
Fig. 5. Comparison of T1W, T1MPRAGE and T1WE. Histograms for T1W (a), T1MPRAGE (b) and T1WE (c) are plotted on the axial images (left image in each row). As is evident from the histograms, the T1WE has better GM/WM separation compared to T1W and T1MPRAGE.

quired rapidly helps to reduce misregistration artifacts. The preliminary results acquired on ten healthy subjects did not show obvious motion between scans, and image registration was not necessary. The improved contrast in the T1WE images should improve the ability of current automatic segmentation algorithms since the conventional T1 MPRAGE are normally the primary images used in this process. In this study, the measured CNR for WM to deep GM demonstrated this point that the T1WE images have much better CNR than T1MPRAGE because the deep GM region (at the center of the image and slice locations) has the highest k value around 1.2. That is also the reason for that the measured CNR for WM to deep GM on T1MPRAGE is very small (Fig. 7).

The signal level on putamen is close (or even higher for some subjects) to the WM region. Whereas the T1W from a large FA (close to TR at 3T) scan usually has less B_{1t} effect than a scan with a small FA.

The increased GM/WM contrast on the T1WE is from the subtraction of the two signals the high flip angle data having WM brighter than GM and the low flip angle data having WM darker than GM. The choice of angles is quite flexible if the only condition is to remain within the 90% maximum range. We chose 6° to keep the SNR of the low flip angle as high as possible and 24° to keep SAR effects minimal. Slightly large FAs would increase the SNR in the image a little bit but at the expense of higher SAR.
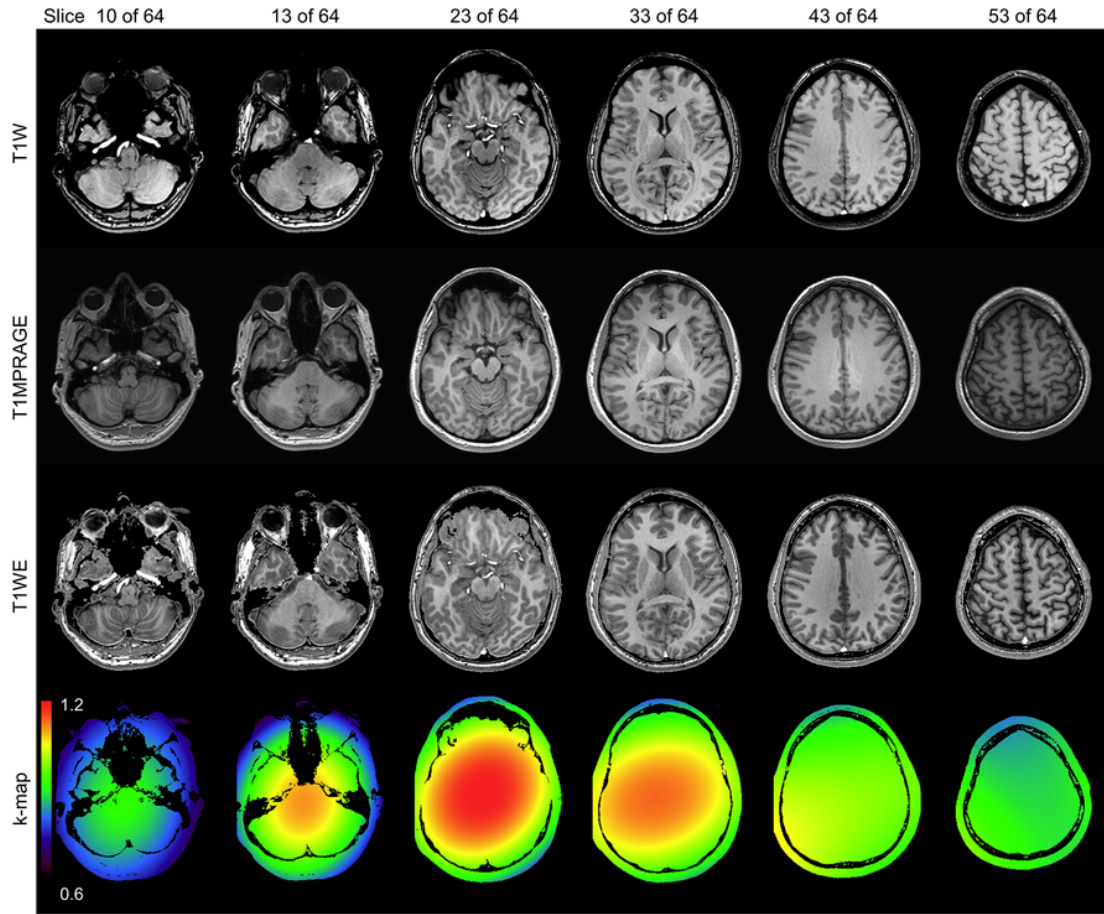
Fig. 6. Comparison of acquired T1W (first row), T1MPRAGE (second row) and T1WE (third row) on a healthy subject at different slice locations. Images at each row have the same window and level. T1WE has better GM/WM contrast and in-plane/through-plane image homogeneity after correcting for the RF transmit variations using the extracted k-map (fourth row) than either T1W or T1MPRAGE.
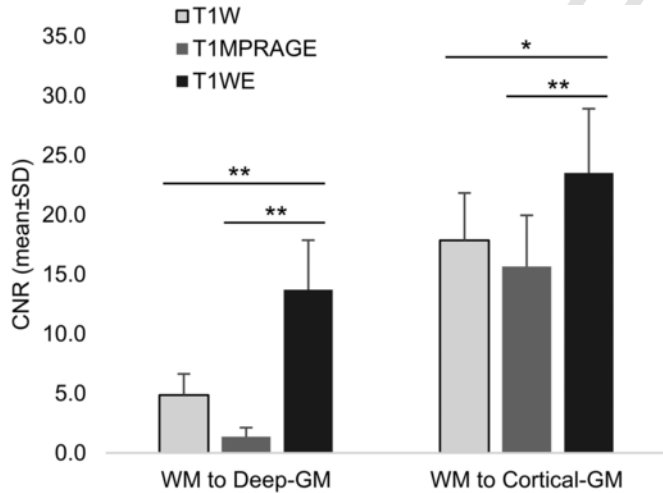

Fig. 7. CNR comparison between T1W, T1MPRAGE and T1WE. The proposed T1WE has a significant CNR increase compared to T1W and T1MPRAGE on both WM to deep GM and WM to cortical GM. Measured CNRs using Eq. (2) with σ_0 from the WM ROI are presented as mean $\pm$ SD across the ten datasets.

The four echo times used in these two scans proved valuable in avoiding phase aliasing and reducing phase unwrapping times. Generally, a phase image with a shorter echo time is easier to unwrap than a longer echo time as the latter normally has more phase aliasing than the former. For some cases with high iron content or hemorrhage, a longer echo time can lead to artifacts on QSM and in this case it can be out-performed in terms of image quality using the short echo time of 7.5 ms [49,56]. Furthermore, the short echo of 7.5 ms itself can be used for SWI and QSM for thrombosis, cerebral microbleeds and hemorrhage cases [23,26]. The proposed weighted-average ME-QSM compared to the single echo result also has an increase in both SNR and CNR. The SNR and CNR increases are both from the increased susceptibility values for basal ganglia structures and decreased image background noise SD from the weighted-average. There is also a constant phase term present that is extracted by complex dividing the two times of the unwrapped phase at 8.75 ms by the unwrapped phase at 17.5 ms and then subtracted from the phase of all echoes. The lower FA data provides a magnitude image with only slightly suppressed CSF and this leads to a better delineation of veins in the SWI data than the larger FA data.

There are a few limitations in this study. First, the effects of motion and misregistration of the two FA data sets were not considered, although this can be handled with motion correction when necessary; second, two FA data can be used to generate not only T1 and PD maps but also simulate other types of contrast, although our T1WE images have theoretically better contrast than any single FA simulated data; third, the T1 mapping using two FAs could fail for some pathological cases with enlarged ventricles or with extra-large space-occupying lesions; and fourth the reconstruction time was prolonged due to the four different echoes for the QSM reconstructions, although this is partly compensated by the rapid phase unwrapping approach used here. Finally, although STAGE provides for the creation of various image contrasts, from a clinical perspective it is important to collect either a T2W
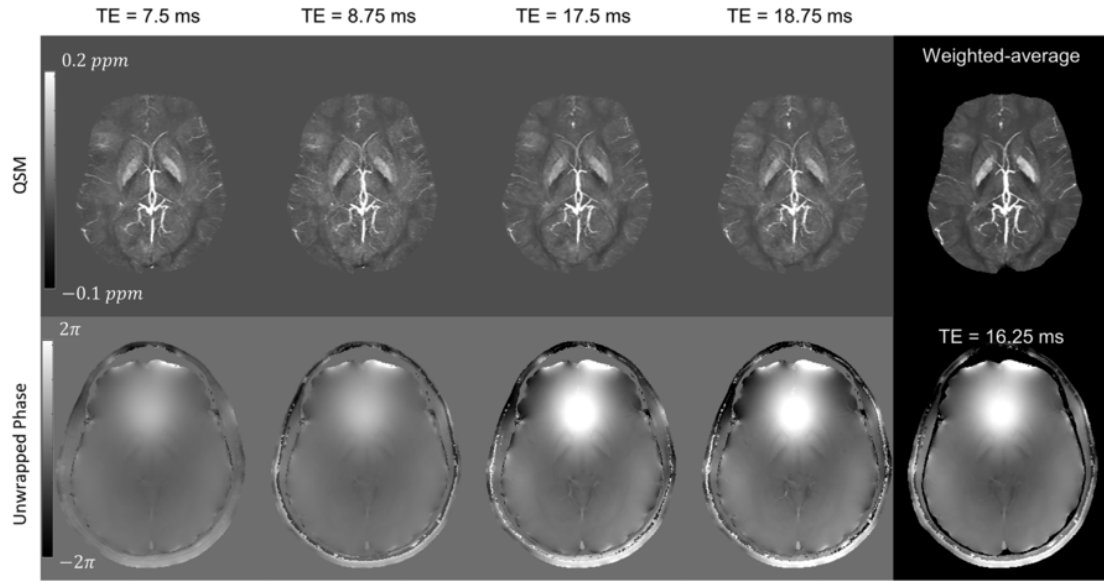
Fig. 8. ME-QSM and unwrapped phase images from a 27-year-old male volunteer. The weighted-average final QSM (the right image at the end of the first row with dark background) has improved CNR and SNR compared to those from the individual echoes. The second row represents the unwrapped phase using the unwrapping method discussed in the text. The calculated phase at TE = 16.25 ms is shown as the last image in the second row.
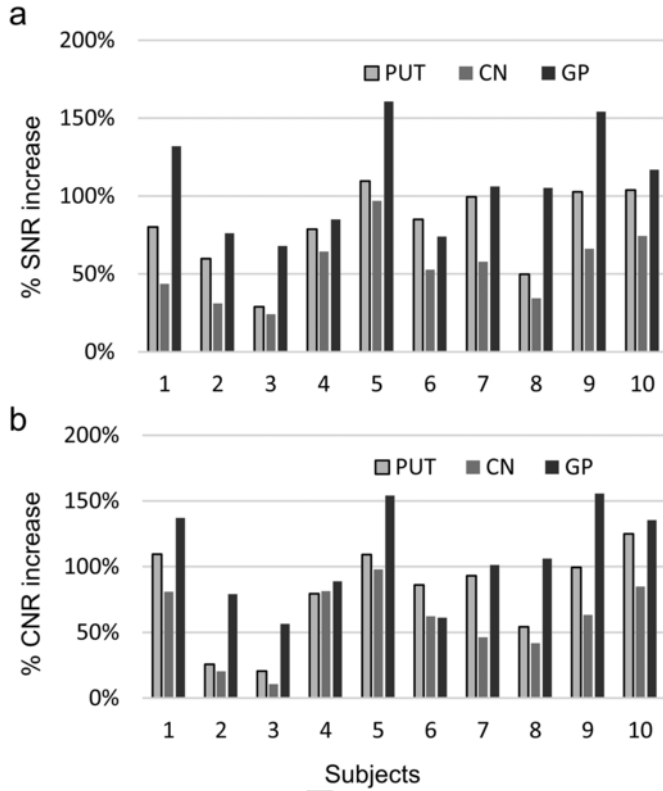

Fig. 9. QSM SNR and CNR changes after performing the weighted-average relative to the TE = 17.5 ms echo. SNR and CNR were measured using Eqs. (9), (10) in which the image noise SD was from the WM ROI.

image or a T2-FLAIR image and a diffusion weighted image. With these last two scans included in the protocol, the total scan time at 3T would be roughly 9 min. All images are set to have a spatial resolution of $0.67 \times 1.33 \times 2.0$ mm^3 with 64 slices covering the whole brain except for the DWI which is usually set to have a resolution of $1.33 \times 1.33 \times 4.0$ mm^3 with 32 slices. On the other hand, for various study purposes and interests, STAGE is flexible with either a higher or a lower spatial resolution as long as one keeps the resolution parameters, echo asymmetric ratio and the sampling bandwidth the same for the two scans. The in-house automatic processing program took 3 min to generate all the results on a modern laptop which should be further improved for online reconstruction. Gadolinium based pre- and post-T1W was not studied in this work. However, we anticipate the same T1 contrast enhancement by the subtraction of two FAs and for the image inhomogeneity correction by extracted B_{1t} field map.

5. Conclusions

STAGE is a rapid imaging approach producing whole brain qualitative and quantitative information including various image contrasts (T1WE, ME-QSM, as well as traditional T1 weighted and PD weighted and RF transmit field corrected T1 maps, PD maps, SWI, tSWI and R2* maps). All these images are acquired in only two scans of 2.5 min each at 3T covering the whole brain. The standardization of a brain imaging protocol like STAGE has the potential to provide both qualitative and quantitative information that should be comparable across manufacturers and field strengths in a clinically practical scan time.
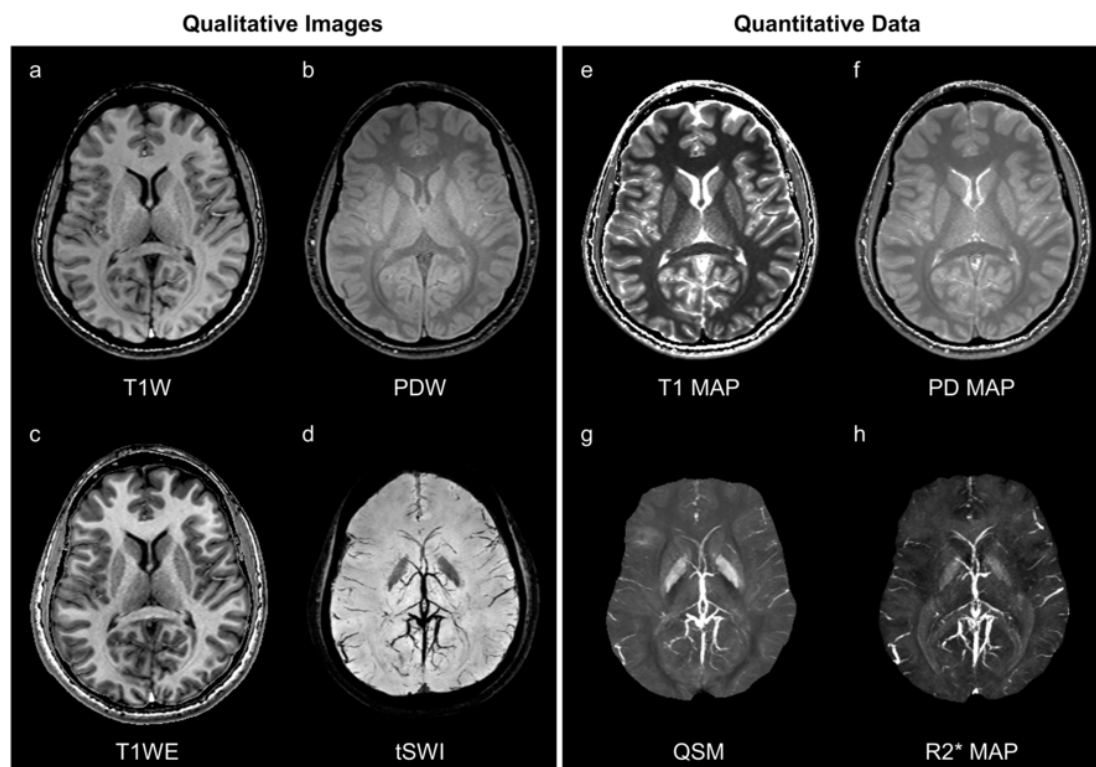
Fig. 10. STAGE results from a 27-year-old male volunteer acquired in 5 min at 3 T including qualitative images and quantitative data. Images a and b are acquired data. All other images are processed data. Images d, g and h are minimum/maximum intensity projections over 8 slices with an effective slice thickness of 16 mm.

References

[1] A. Haase, J. Frahm, D. Matthaei, W. Hanicke, K.-D. Merboldt, FLASH imaging. Rapid NMR imaging using low flip-angle pulses, J Magn Reson 67 (1986) 258–266.

[2] E.M. Haacke, R.W. Brown, M.R. Thompson, R. Venkatesan, Magnetic resonance imaging: physical principles and sequence design, 1st ed., Wiley-Liss, New York, 1999.

[3] J.P. Mugler, J.R. Brookeman, Three-dimensional magnetization-prepared rapid gradient-echo imaging (3D MP RAGE), Magn Reson Med 15 (1990) 152–157.

[4] D.S. Gierada, J.J. Curtin, S.J. Erickson, R.W. Prost, J.A. Strandt, L.R. Goodman, Diaphragmatic motion: fast gradient-recalled-echo MR imaging in healthy subjects, Radiology 194 (1995) 879–884.

[5] T. Kurki, M. Komu, Spin-lattice relaxation and magnetization transfer in intracranial tumors in vivo: effects of Gd-DTPA on relaxation parameters, Magn Reson Imaging 13 (1995) 379–385.

[6] V.L. Stevenson, G.J.M. Parker, G.J. Barker, K. Birnie, P.S. Tofts, D.H. Miller, et al., Variations in T1 and T2 relaxation times of normal appearing white matter and lesions in multiple sclerosis, J Neurol Sci 178 (2000) 81–87.

[7] L. Vaithianathar, C.R. Tench, P.S. Morgan, C.S. Constantinescu, Magnetic resonance imaging of the cervical spinal cord in multiple sclerosis, J Neurol 250 (2003) 307–315.

[8] L.E. Ginsberg, G.N. Fuller, M. Hashmi, N.E. Leeds, D.F. Schomer, The significance of lack of MR contrast enhancement of supratentorial brain tumors in adults: histopathological evaluation of a series, Surg Neurol 49 (1998) 436–440.

[9] M. Bergamino, L. Bonzano, F. Levrero, G.L. Mancardi, L. Roccatagliata, A review of technical aspects of T1-weighted dynamic contrast-enhanced magnetic resonance imaging (DCE-MRI) in human brain tumors, Phys Med 30 (2014) 635–643.

[10] M. Filippi, M.A. Rocca, O. Ciccarelli, N. De Stefano, N. Evangelou, L. Kappos, et al., MRI criteria for the diagnosis of multiple sclerosis: MAGNIMS consensus guidelines, Lancet Neurol 15 (2016) 292–303.

[11] D.M. Wingerchuk, J.L. Carter, Multiple sclerosis: current and emerging disease-modifying therapies and treatment strategies, Mayo Clin Proc 89 (2014) 225–240, (Elsevier).

[12] S.J.C.G. Hectors, I. Jacobs, C.T.W. Moonen, G.J. Strijkers, K. Nicolay, MRI methods for the evaluation of high intensity focused ultrasound tumor treatment: current status and future needs, Magn Reson Med 75 (2016) 302–317.

[13] J.R. Reichenbach, R. Venkatesan, D.J. Schillinger, D.K. Kido, E.M. Haacke, Small vessels in the human brain: MR venography with deoxyhemoglobin as an intrinsic contrast agent, Radiology 204 (1997) 272–277.

[14] E.M. Haacke, Y. Xu, Y.C. Cheng, J.R. Reichenbach, Susceptibility weighted imaging (SWI), Magn Reson Med 52 (2004) 612–618, https://doi.org/10.1002/mrm.20198.

[15] E.M. Haacke, S. Mittal, Z. Wu, J. Neelavalli, Y.C. Cheng, Susceptibility-weighted imaging: technical aspects and clinical applications, part 1, AJNR Am J Neuroradiol 30 (2009) 19–30, https://doi.org/10.3174/ajnr.A1400.

[16] K.A. Tong, S. Ashwal, B.A. Holshouser, L.A. Shutter, G. Herigault, E.M. Haacke, et al., Hemorrhagic shearing lesions in children and adolescents with posttraumatic diffuse axonal injury: improved detection and initial results 1, Radiology 227 (2003) 332–339.

[17] S. Mittal, Z. Wu, J. Neelavalli, E.M. Haacke, Susceptibility-weighted imaging: technical aspects and clinical applications, part 2, Am J Neuroradiol 30 (2009) 232–252.

[18] E.M. Haacke, Z.S. DelProposto, S. Chaturvedi, V. Sehgal, M. Tenzer, J. Neelavalli, et al., Imaging cerebral amyloid angiopathy with susceptibility-weighted imaging, Am J Neuroradiol 28 (2007) 316–317.

[19] K.A. Tong, S. Ashwal, A. Obenaus, J.P. Nickerson, D. Kido, E.M. Haacke, Susceptibility-weighted MR imaging: a review of clinical applications in children, Am J Neuroradiol 29 (2008) 9–17.

[20] M. Ayaz, A.S. Boikov, E.M. Haacke, D.K. Kido, W.M. Kirsch, Imaging cerebral microbleeds using susceptibility weighted imaging: one step toward detecting vascular dementia, J Magn Reson Imaging 31 (2010) 142–148.

[21] C. Cordonnier, W.M. van der Flier, Brain microbleeds and Alzheimer's disease: innocent observation or key player?, Brain 134 (2011) 335–344.

[22] E.M. Haacke, J.R. Reichenbach, Susceptibility weighted imaging in MRI: basic concepts and clinical applications, John Wiley & Sons, 2014.

[23] S. Liu, S. Buch, Y. Chen, H. Choi, Y. Dai, C. Habib, et al., Susceptibility-weighted imaging: current status and future directions, NMR Biomed (2016).

[24] S. Buch, Y.N. Cheng, J. Hu, S. Liu, J. Beaver, R. Rajagovindan, et al., Determination of detection sensitivity for cerebral microbleeds using susceptibility-weighted imaging, NMR Biomed 30 (2017).

[25] L. de Rochefort, T. Liu, B. Kressler, J. Liu, P. Spincemaille, V. Lebon, et al., Quantitative susceptibility map reconstruction from MR phase data using bayesian regularization: validation and application to brain imaging, Magn Reson Med 63 (2010) 194–206.

[26] E.M. Haacke, S. Liu, S. Buch, W. Zheng, D. Wu, Y. Ye, Quantitative susceptibility mapping: current status and future directions, Magn Reson Imaging 33 (2015) 1–25, https://doi.org/10.1016/j.mri.2014.09.004.

[27] Y. Wang, P. Spincemaille, Z. Liu, A. Dimov, K. Deh, J. Li, et al., Clinical quantitative susceptibility mapping (QSM): biometal imaging and its emerging roles in patient care, J Magn Reson Imaging (2017).

[28] C. Liu, W. Li, K.A. Tong, K.W. Yeom, S. Kuzminski, Susceptibility-weighted imaging and quantitative susceptibility mapping in the brain, J Magn Reson Imaging 42 (2015) 23–41.

[29] Y. Wang, T. Liu, Quantitative susceptibility mapping (QSM): decoding MRI data for a tissue magnetic biomarker, Magn Reson Med 73 (2015) 82–101.

[30] S. Xia, G. Zheng, W. Shen, S. Liu, L.J. Zhang, E.M. Haacke, et al., Quantitative measurements of brain iron deposition in cirrhotic patients using susceptibility mapping, Acta Radiol 56 (2015) 339–346.

[31] B. Bilgic, A. Pfefferbaum, T. Rohlfing, E.V. Sullivan, E. Adalsteinsson, MRI estimates of brain iron concentration in normal aging using quantitative susceptibility mapping, NeuroImage 59 (2012) 2625–2635.

[32] Deoni SCL, T.M. Peters, B.K. Rutt, High-resolution T1 and T2 mapping of the brain in a clinically acceptable time with DESPOT1 and DESPOT2, Magn Reson Med 53 (2005) 237–241.

[33] S.C.L. Deoni, High-resolution T1 mapping of the brain at 3 T with driven equilibrium single pulse observation of T1 with high-speed incorporation of RF field inhomogeneities (DESPOT1-HIFI), J Magn Reson Imaging 26 (2007) 1106–1111.

[34] J.B.M. Warntjes, O. Dahlqvist, P. Lundberg, Novel method for rapid, simultaneous T1, T* 2, and proton density quantification, Magn Reson Med 57 (2007) 528–537.

[35] J.B.M. Warntjes, O.D. Leinhard, J. West, P. Lundberg, Rapid magnetic resonance quantification on the brain: Optimization for clinical usage, Magn Reson Med 60 (2008) 320–329.

[36] M.J.B. Warntjes, J. Kihlberg, J. Engvall, Rapid T 1 quantification based on 3D phase sensitive inversion recovery, BMC Med Imaging 10 (2010) 19.

[37] I. Blystad, J.B.M. Warntjes, O. Smedby, A.-M. Landtblom, P. Lundberg, E.-M. Larsson, Synthetic MRI of the brain in a clinical setting, Acta Radiol 53 (2012) 1158–1163.

[38] D. Ma, V. Gulani, N. Seiberlich, K. Liu, J.L. Sunshine, J.L. Duerk, et al., Magnetic resonance fingerprinting, Nature 495 (2013) 187–192.

[39] Y. Jiang, D. Ma, N. Seiberlich, V. Gulani, M.A. Griswold, MR fingerprinting using fast imaging with steady state precession (FISP) with spiral readout, Magn Reson Med 74 (2015) 1621–1631.

[40] R.A. Heckemann, J.V. Hajnal, P. Aljabar, D. Rueckert, A. Hammers, Automatic anatomical brain MRI segmentation combining label propagation and decision fusion, NeuroImage 33 (2006) 115–126.

[41] B. Fischl, D.H. Salat, E. Busa, M. Albert, M. Dieterich, C. Haselgrove, et al., Whole brain segmentation: automated labeling of neuroanatomical structures in the human brain, Neuron 33 (2002) 341–355.

[42] M. Prastawa, J.H. Gilmore, W. Lin, G. Gerig, Automatic segmentation of MR images of the developing newborn brain, Med Image Anal 9 (2005) 457–466.

[43] S. Liu, K. Mok, J. Neelavalli, Y.C. Cheng, J. Tang, Y. Ye, et al., Improved MR venography using quantitative susceptibility-weighted imaging, J Magn Reson Imaging 40 (2014) 698–708, https://doi.org/10.1002/jmri.24413.

[44] J. Homer, M.S. Beevers, Driven-equilibrium single-pulse observation of T1 relaxation. A reevaluation of a rapid "new" method for determining NMR spin-lattice relaxation times, J Magn Reson 63 (1985) 287–297.

[45] E.K. Fram, R.J. Herfkens, G.A. Johnson, G.H. Glover, J.P. Karis, A. Shimakawa, et al., Rapid calculation of T1 using variable flip angle gradient refocused imaging, Magn Reson Imaging 5 (1987) 201–208.

[46] N. Weiskopf, A. Lutti, G. Helms, M. Novak, J. Ashburner, C. Hutton, Unified segmentation based correction of R1 brain maps for RF transmit field inhomogeneities (UNICORT), NeuroImage 54 (2011) 2116–2124.

[47] S. Baudrexel, S.C. Reitz, S. Hof, R. Gracien, V. Fleischer, H. Zimmermann, et al., Quantitative T1 and proton density mapping with direct calculation of radiofrequency coil transmit and receive profiles from two-point variable flip angle data, NMR Biomed 29 (2016) 349–360.

[48] D. Wu, S. Liu, S. Buch, Y. Ye, Y. Dai, E.M. Haacke, A fully flow-compensated multiecho susceptibility-weighted imaging sequence: the effects of acceleration and background field on flow compensation, Magn Reson Med 76 (2016) 478–489, https://doi.org/10.1002/mrm.25878.

[49] R. Rastogi, Y. Ding, S. Xia, M. Wang, Y. Luo, H.S. Choi, et al., Recent advances in magnetic resonance imaging for stroke diagnosis, Brain Circ 1 (2015) 26–37.

[50] S.C.L. Deoni, B.K. Rutt, T.M. Peters, Rapid combined T1 and T2 mapping using gradient recalled acquisition in the steady state, Magn Reson Med 49 (2003) 515–526.

[51] H.S. Abdul-Rahman, M.A. Gdeisat, D.R. Burton, M.J. Lalor, F. Lilley, C.J. Moore, Fast and robust three-dimensional best path phase unwrapping algorithm, Appl Opt 46 (2007) 6623–6635.

[52] S.M. Smith, Fast robust automated brain extraction, Hum Brain Mapp 17 (2002) 143–155.

[53] S. Witoszynskyj, A. Rauscher, J.R. Reichenbach, M. Barth, Phase unwrapping of MR images using ΦUN–A fast and robust region growing algorithm, Med Image Anal 13 (2009) 257–268.

[54] F. Schweser, A. Deistung, B.W. Lehr, J.R. Reichenbach, Quantitative imaging of intrinsic magnetic tissue properties using MRI signal phase: an approach to in vivo brain iron metabolism?, NeuroImage 54 (2011) 2789–2807.

[55] E.M. Haacke, J. Tang, J. Neelavalli, Y.C.N. Cheng, Susceptibility mapping as a means to visualize veins and quantify oxygen saturation, J Magn Reson Imaging 32 (2010) 663–676.

[56] S. Xia, D. Utriainen, J. Tang, Z. Kou, G. Zheng, X. Wang, et al., Decreased oxygen saturation in asymmetrically prominent cortical veins in patients with cerebral ischemic stroke, Magn Reson Imaging 32 (2014) 1272–1276, https://doi.org/10.1016/j.mri.2014.08.012.